

Article

Synthesis and Characterization of Titanium Nitride–Carbon Composites and Their Use in Lithium-Ion Batteries

Helia Magali Morales ^{1,2}, Horacio Vieyra ² , David A. Sanchez ³, Elizabeth M. Fletes ³, Michael Odlyzko ⁴, Timothy P. Lodge ^{5,6} , Victoria Padilla-Gainza ³ , Mataz Alcoutlabi ³  and Jason G. Parsons ^{7,*} 

- ¹ School of Integrative Biological and Chemical Sciences, University of Texas Rio Grande Valley, 1 West University Blvd., Brownsville, TX 78521, USA; helia.morales@utrgv.edu
- ² School of Engineering and Sciences, Tecnologico de Monterrey, Av. E. Garza Sada 2501, Monterrey 64849, NL, Mexico; h.vieyra@tec.mx
- ³ Department of Mechanical Engineering, University of Texas Rio Grande Valley, 1201 West University Dr., Edinburg, TX 78539, USA; david.sanchez11@utrgv.edu (D.A.S.); elizabeth.fletes01@utrgv.edu (E.M.F.); mataz.alcoutlabi@utrgv.edu (M.A.)
- ⁴ Characterization Facility, College of Science and Engineering, 55 Shepherd Laboratories, University of Minnesota, Minneapolis, MN 55455, USA; odlyz003@umn.edu
- ⁵ Department of Chemical Engineering and Materials Science, University of Minnesota, Minneapolis, MN 55455, USA; lodge@umn.edu
- ⁶ Department of Chemistry, University of Minnesota, Minneapolis, MN 55455, USA
- ⁷ School of Earth Environmental and Marine Sciences, University of Texas Rio Grande Valley, 1 West University Blvd., Brownsville, TX 78521, USA
- * Correspondence: jason.parsons@utrgv.edu; Tel.: +1-(956)882-7772

Abstract: This work focuses on the synthesis of titanium nitride–carbon (TiN–carbon) composites by the thermal decomposition of a titanyl phthalocyanine (TiN(TD)) precursor into TiN. The synthesis of TiN was also performed using the sol-gel method (TiN(SG)) of an alkoxide/urea. The structure and morphology of the TiN–carbon and its precursors were characterized by XRD, FTIR, SEM, TEM, EDS, and XPS. The FTIR results confirmed the presence of the titanium phthalocyanine (TiOPC) complex, while the XRD data corroborated the decomposition of TiOPC into TiN. The resultant TiN exhibited a cubic structure with the FM3–M lattice, aligning with the crystal system of the synthesized TiN via the alkoxide route. The XPS results indicated that the particles synthesized from the thermal decomposition of TiOPC resulted in the formation of TiN–carbon composites. The TiN particles were present as clusters of small spherical particles within the carbon matrix, displaying a porous sponge-like morphology. The proposed thermal decomposition method resulted in the formation of metal nitride composites with high carbon content, which were used as anodes for Li-ion half cells. The TiN–carbon composite anode showed a good specific capacity after 100 cycles at a current density of 100 mA^g^{−1}.

Keywords: thermal decomposition; titanyl phthalocyanine; LIBs; TiN; TiN–carbon composite



Citation: Morales, H.M.; Vieyra, H.; Sanchez, D.A.; Fletes, E.M.; Odlyzko, M.; Lodge, T.P.; Padilla-Gainza, V.; Alcoutlabi, M.; Parsons, J.G. Synthesis and Characterization of Titanium Nitride–Carbon Composites and Their Use in Lithium-Ion Batteries. *Nanomaterials* **2024**, *14*, 624. <https://doi.org/10.3390/nano14070624>

Academic Editors: Juan Carlos Calderón Gómez and Alejandro González Orive

Received: 9 March 2024

Revised: 25 March 2024

Accepted: 31 March 2024

Published: 2 April 2024



Copyright: © 2024 by the authors. Licensee MDPI, Basel, Switzerland. This article is an open access article distributed under the terms and conditions of the Creative Commons Attribution (CC BY) license (<https://creativecommons.org/licenses/by/4.0/>).

1. Introduction

The development of new renewable energy sources has been driven by the rapidly growing market for mobile electronic devices as well as hybrid and electric vehicles, which require highly efficient, low-cost, and environmentally friendly energy storage technologies [1,2]. Lithium-ion batteries (LIBs) have been the dominant power source for both portable electronics and electric vehicles [3]. These technologies are promising for large-scale energy storage because of their superior performance, high energy density, high specific power, long cycle life, small memory effects, low self-discharge rate, environmental friendliness, and low mass density [4,5].

Extensive research has contributed to enhancing LIB performance, affordability, and safety. These enhancements in LIB technology have been achieved largely through the

improvement of the electrochemical performance of the electrode and separator materials [4,6]. In fact, the electrochemical performance of LIBs depends significantly on the properties and morphology of the electrode materials; thus, the exploration of advanced anode materials has been highly active. In addition to the more traditional intercalation-type materials, diverse alloying and conversion materials offer remarkable potential for use in LIB applications due to their high specific capacities, higher electronic conductivity, and great chemical and thermal stability [4]. Currently, graphite is the most used anode material in commercial LIBs due to its low cost, high abundance, and high cyclability. However, the graphite anode exhibits low theoretical specific capacity (372 mAhg^{-1}) [4]. Therefore, it is crucial to replace the graphite anode.

Recent research has focused on alloying-type anode materials, such as silicon, tin, aluminum, magnesium, silver, iron, and antimony; furthermore, conversion-type materials, such as transition metal dichalcogenides (TMDs), transition metal oxides (TMOs), and transition metal nitrides (TMNs) have also been areas of focus. These new materials have been developed as high-performance anode materials due to their high specific capacities, as well as their chemical and thermal stability [4]. Different strategies, such as morphology control, have been used to improve the electrochemical performance of anode materials. For example, the use of nanowires, nanotubes, core-shell, coral-like, hollow, microspheres, and carbonaceous-based composites have been investigated [2,4,7,8].

The early use of nitrides in LIBs, either as lithium transition metal nitrides or binary transition metal nitrides, showed poor electrochemical performance. However, metal nitrides have attracted considerable attention due to possessing low polarization, low polarization loss, and higher electronic conductivity than transition metal oxides and the formation of Li_3N [9]. Lithium is stored in both the crystalline and amorphous structures of TMNs through a conversion reaction [10]. The products of the conversion reaction for TMOs and TMDs are Li_2O and Li_2S , which are poor conductors; however, the TMNs form Li_3N as a conversion product, which is a superionic conducting material [4,9]. The most used TMN anode materials in LIBs include CoN , TiN , VN , and CrN ; other examined TMNs, such as Zn_3N_2 , Cu_3N , and Ge_3N_4 , have exhibited moderate to poor electrochemical stability [9].

TiN is an attractive material with extensive applications in coatings, catalysis, sensors for electroanalysis, and supercapacitors. Tang et al. coated silicon nanoparticles with TiN to improve the cycling performance of LIBs; the resultant anode material exhibited a reversible specific capacity of 1900 and 400 mAhg^{-1} after 100 cycles at 0.1 C and 2 C charging, respectively [11]. Similarly, Balogun et al. grew TiO_2 nanowires on carbon cloth by a hydrothermal method and subsequent annealing at 800°C under a nitrogen atmosphere [12]. The TiO_2 was coated with a TiN shell, changing the flow to ammonia and keeping the temperature constant at 800°C . The $\text{TiO}_2/\text{TiN}/\text{C}$ composite anode delivered a capacity of 203 mAhg^{-1} after 650 cycles at 10 C. Zheng et al. fabricated titanium nitride nanowires that supported silicon nanorods via radio frequency magnetron sputtering of Si onto the TiN nanowires [13]. After 200 cycles, the composite anode material exhibited a specific capacity of 3258 and 2256 mAhg^{-1} at a current density of 1 and 10 Ag^{-1} , respectively, indicating that the TiN/Si composite can be considered a promising anode material for LIBs. Dong et al. synthesized TiN mesoporous spheres with cyanamide to prevent nanopore collapse during conversion and recrystallization [14]. A mixture of TiO_2 spheres and cyanamide was heated to 800°C under an ammonia atmosphere for 1 h. The energy density of the composite anode was 45.0 WhKg^{-1} at a power density of 150 Wkg^{-1} , showing a potential application as a high-energy capacitor and LIB.

TiN can be synthesized by different methods such as combustion, sol-gel, magnetron sputtering, mechano-synthesis, metathesis, nitridation, ammonolysis, laser nitridation, carbothermal reduction–nitridation, electrochemically, chemical vapor deposition, physical vapor deposition, and thermal decomposition [15–27]. Several of these methods, which include high temperatures and long synthesis times, are either challenging or expensive [28]. However, metal–organic compounds have been valuable sacrificial templates to prepare metal-based nanoparticles dispersed in a carbon matrix [29]. The selection

of the starting materials allows control over the resultant structure, generating materials with high porosity and high surface area, as well as improved electrochemical properties. Metal-substituted phthalocyanines are well-known conjugated macrocycles that form two-dimensional layered structures. This class of compounds has been shown to produce metal nitride/amorphous carbon composites [30].

The main goal of the present work is the synthesis and characterization of TiN(TD) by the thermal decomposition of titanyl phthalocyanine precursor as well as the possibility of using TiN/C composite as an anode for LIBs. The current manuscript discusses in detail the synthesis and characterization of TiN as well as the synthesis of carbon from the H₂PC. Further work will be conducted to investigate the electrochemical performance of these materials.

The present work focuses on the use of a one-step pyrolysis method based on the thermal decomposition of TiOPC to synthesize a TiN–carbon composite. For comparative purposes, TiN was also prepared using an alkoxide method with urea as the nitrogen source to verify the synthesis. The structure and morphology of the resultant materials were characterized by XRD, FTIR, SEM, TEM, EDS, and XPS. The TiN–carbon composite materials were then used as anodes in LIBs, and their electrochemical performance was evaluated by CV and galvanostatic charge-discharge measurements.

2. Methods

2.1. Materials Synthesis

All the reagents were of analytical grade and used without further purification. The TiOPC precursor for the generation of the TiN–carbon composite (TiN(TD)) was prepared by refluxing TiCl₄ with phthalonitrile in a 4:1 ratio in 1-chloronaphthalene for 6 h [31]. After the reaction, the mixture was cooled to room temperature and the product was obtained by vacuum filtration. The sample was washed with methanol and acetone and further purified by sublimation. After purification and drying, the TiOPC was placed in an alumina crucible and loaded into a quartz tube in a Thermolyne horizontal tube furnace (model F79330-33-70) (Thermo Fisher Scientific, Waltham, MA, USA). The quartz tube was sealed and purged with nitrogen (UHP) for 15 min. The temperature of the furnace was increased from room temperature to 750 °C at a rate of 10 °C min^{−1} and maintained at 750 °C for 5 h. After the reaction, the samples were allowed to cool to room temperature while maintaining the nitrogen flow. For comparison purposes, the H₂PC was also synthesized using the same reaction conditions, without the presence of TiCl₄, and then was carbonized using the same conditions to prepare carbon (H₂PC(TD)). The TiN was prepared using a sol-gel method (TiN(SG)) [16]. In brief, 2.25 g of urea was dissolved in 5 mL of ethanol, and 1 mL of TiCl₄ was added slowly under magnetic stirring. The resultant gel was poured into an alumina crucible and placed in a quartz tube in a horizontal tube furnace. The quartz tube was sealed and purged with nitrogen for 15 min. The temperature of the furnace was increased from room temperature to 750 °C at a rate of 10 °C min^{−1} and then maintained for 5 h. After 5 h of reaction, the sample was cooled to room temperature naturally while maintaining the nitrogen flow.

2.2. Characterization

The synthesized compounds were characterized by FTIR, XRD, SEM, TEM, and XPS. FTIR spectra of the dried and ground species were collected using a Perkin-Elmer Frontier FTIR spectrometer equipped with an attenuated total reflection (ATR) accessory. The spectra were collected over the range of 4000–650 cm^{−1}, collecting 32 scans at a resolution of 4 cm^{−1}. The data were analyzed using Spectrum software (Version 8.0, Perkin Elmer, Waltham, MA, USA). The XRD data were collected using a Bruker D2 phaser diffractometer with a cobalt source ($K_{\alpha} = 1.789 \text{ \AA}$) and an iron filter. The materials were prepared by homogenizing samples into fine powders using a mortar and pestle. The patterns were collected from 10 to 80° 2 θ with a 0.05° step size and 5 s counting time. The collected diffraction patterns were fitted using the Le Bail fitting procedure in the FullProf Suit software (Version 5.10) and crystallographic data from the literature [32–35].

The product morphology was observed using SEM. The SEM images were collected using a Sigma VP Carl Zeiss scanning electron microscope (Carl Zeiss, White Plains, NY, USA). The SEM was operated with accelerating voltages between 2.0 and 6.0 kV at a working distance of up to 6.5 mm. The SEM was equipped with an EDS from EDAX model Octane Super (EDAX, Pleasanton, CA, USA) and was used to determine the elemental distribution of C, O, N, and Ti in the synthesized samples. TEM images were taken using a FEI Titan G2 60-300 (Thermo Fisher Scientific, Waltham, MA, USA) microscope operated with an accelerating voltage of 200 kV. The samples were further analyzed using XPS to determine the surface chemistry of the samples. The XPS data were collected using a Thermo Scientific K-Alpha Photoelectron Spectrometer (Thermo Fisher Scientific, Waltham, MA, USA) and analyzed using the CASA XPS software (Version 2.3.25, Casa Software limited, Teignmouth, UK) [36]. The operation parameters were as follows: a micro-fused monochromatic Al K- α (1486.7 eV) source with scans at 0.1 eV and a spot size of 400 μm .

The CV of the anodes was evaluated using Li-ion half-cells (CR2032 coin cells, PHD Energy Inc., Georgetown, TX, USA). The electrodes were fabricated through a slurry-coating process. The slurry was prepared by mixing 90% of the active material and 10% (mass/mass) polyacrylonitrile (PAN) as the binder in dimethylformamide. A thin film of the mixed slurry was applied onto a 0.025 m thick copper foil and placed in a vacuum oven to be dried at 60 °C for 24 h. The dried coated copper foil was placed in an argon gas-filled tube furnace and heated to 450 °C for 5 h to pyrolyze the PAN binder. The electrodes were punched into 0.5'' diameter discs using a precision punch (Nagomi). Lithium metal was used as the counter electrode (0.38 mm thick, Sigma Aldrich, Rockville, MD, USA) with a glass-fiber separator (Separion S240 P25, 25 μm thickness) (Evonik Industries, Austin, TX, USA). The electrolyte used was 1 M LiPF_6 dissolved in 1:1 (*v/v*) ethylene carbonate/dimethyl carbonate. The cells were assembled in a glovebox (Mbraun, Stratham, NH, USA) under a high-purity argon atmosphere (water and oxygen level < 0.5 ppm). CV experiments were performed at a scan rate of 0.2 mV s^{-1} over a voltage range between 0.05 and 3.0 V (Biologic Science Instruments, Seyssinet-Pariset, France). The electrochemical performance of the electrodes was evaluated by galvanostatic charge-discharge experiments using a LANHE battery testing system (CT2001A) with an applied current density of 100 mA g^{-1} over 100 cycles over the potential range of 0.05–3.0 V.

3. Results and Discussion

3.1. FTIR

Figure 1A,B shows the FTIR spectra collected for the TiOPC and metal-free phthalocyanine (H_2PC) compounds, while Table 1 illustrates the identified FTIR bands. Figure 1B shows an expanded view of the FTIR from 1700 to 650 cm^{-1} .

Table 1. FTIR band position and respective assignments for the H_2PC and TiOPC.

H_2PC Band Position (cm^{-1})	TiOPC Band Position (cm^{-1})	Assignment
710		C-N [37]
729	724	C-H out of plane deformation [38,39]
762	751	Macrocyclic ring stretching [c] [37]
778	778	C-N stretching [38]
	798	N-Ti stretching [37]
839	832	C-N-C ring breathing
872	877	N-H stretching coupling with isoindole deformation [37]
	889	Isoindole deformation with coupling aza stretching [37]
944		

Table 1. Cont.

H ₂ PC Band Position (cm ⁻¹)	TiOPC Band Position (cm ⁻¹)	Assignment
	961	Ti=O [31,37,40]
998	1002	Benzene ring and C=C [37]
1064	1062	C-N stretching in pyrrole vibration [38]
1075		
1091		
1116	1117	C-H in-plane deformation [37–39]
1157	1158	C-N in-plane and C-H in-plane [38,41]
1187		Isoindole stretching [38]
1275		
1299	1286	C-N in isoindole stretching [37,38]
1324		
1336	1330	C-C in isoindole [38]
1417	1413	Isoindole stretching [37]
1437		
1461	1460	C-H in-plane bending [38]
1477	1474	C=N pyrrole [37]
1501	1489	C-H bending in aryl [38]
1523		C-H aryl [38]
1576		
1595	1585	Benzene C-C stretching [42]
1610	1609	C-C stretching vibration in pyrrole [38]
2923	2923	C-H stretching [38]
3004	3004	C-H stretching [38]
3050	3050	C-H stretching vibration in ring [38]
3282		N-H [38]

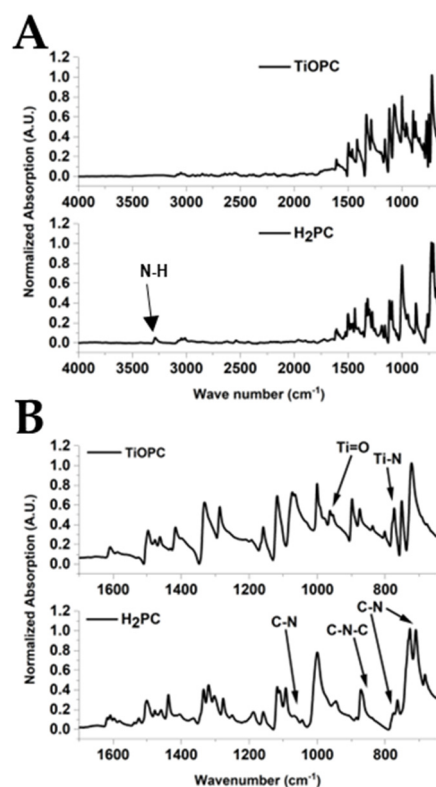


Figure 1. (A) FTIR spectra of the synthesized TiOPC and H₂PC starting materials. (B) Expanded view of FTIR from 1700 to 650 cm⁻¹.

The FTIR spectra of the synthesized compounds showed characteristic bands to confirm the H₂PC and TiOPC. The FTIR results confirmed the synthesis of TiOPC, where the bands at 798 cm⁻¹ and 961 cm⁻¹ indicated the presence of N-Ti-N [38] and Ti=O, respectively [37,40,41]. The N-H stretches observed at 3282 cm⁻¹ in H₂PC were absent in the TiOPC complex, indicating the loss of the N-H and the formation of the Ti-N bonds. In addition, the C-N stretches in TiOPC were shifted to a lower wavenumber than observed for H₂PC, indicating a change in the coordination environment and the formation of Ti-N bonds in the complex [37,38].

3.2. SEM/EDS

SEM was used to study the morphology of synthesized materials. Figure 2A shows the SEM images of TiN synthesized by the sol-gel method (TiN(SG)), with an appearance of homogeneously stacked particles. The SEM image of TiN(TD) in Figure 2B indicates the presence of numerous rough-texture spheres of TiN evenly distributed throughout a tightly packed carbon material.

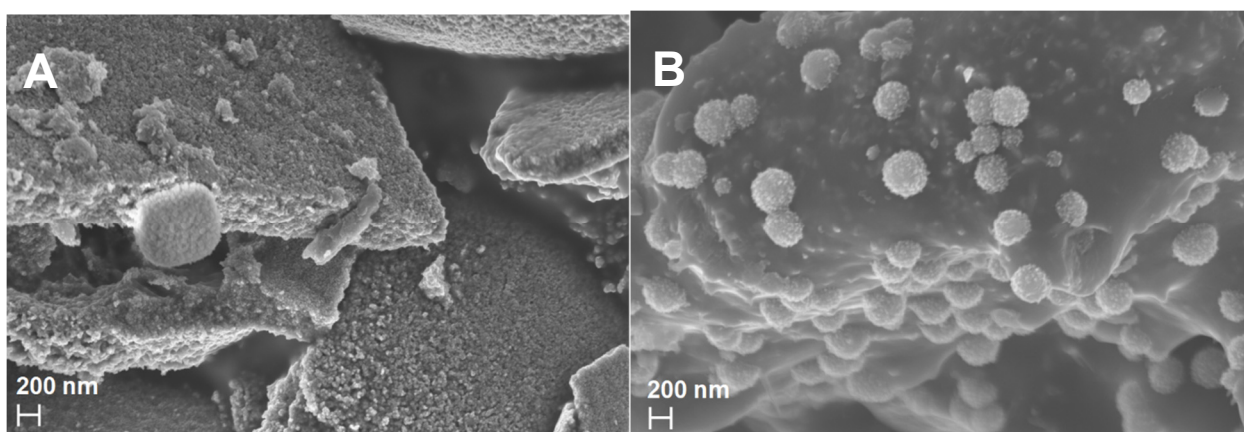


Figure 2. SEM images of (A) TiN(SG) and (B) TiN(TD).

3.3. TEM

Figure 3 shows high-resolution TEM images of TiN(TD). Figure 3A shows that the TiN appears in small clusters throughout the carbon matrix, while Figure 3B reveals a uniform distribution of the TiN nanocrystals within the clusters. The average grain size was determined to be between 3–4 nm.

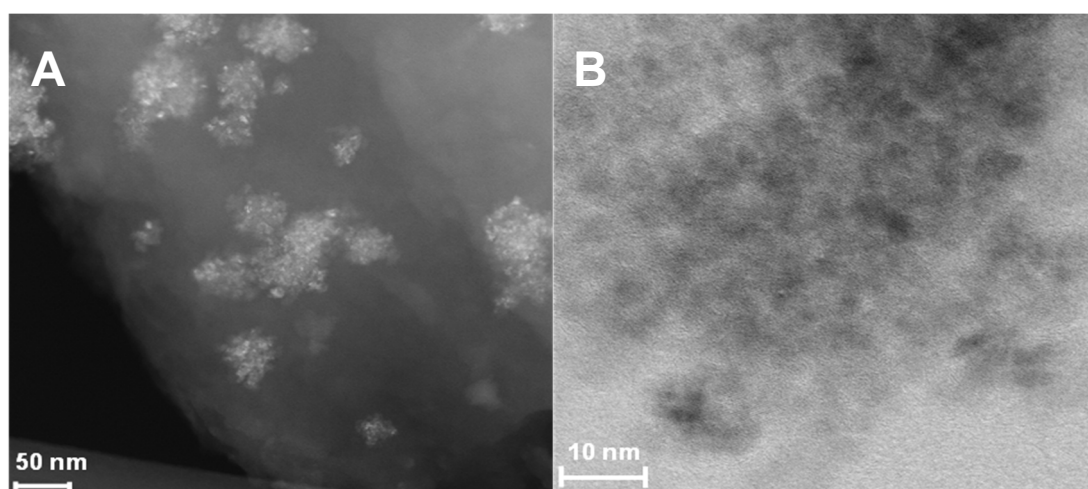


Figure 3. High-resolution TEM images of TiN(TD).

3.4. XRD

Titanium Compounds

The diffraction patterns of TiOPC, TiN(SG), and TiN(TD) are shown in Figure 4. Table 2 shows the Le Bail fitting of the titanium compounds [35]. It should be noted in the Le Bail fitting that the values of χ^2 are below 5, indicating very good fits to the experimental data.

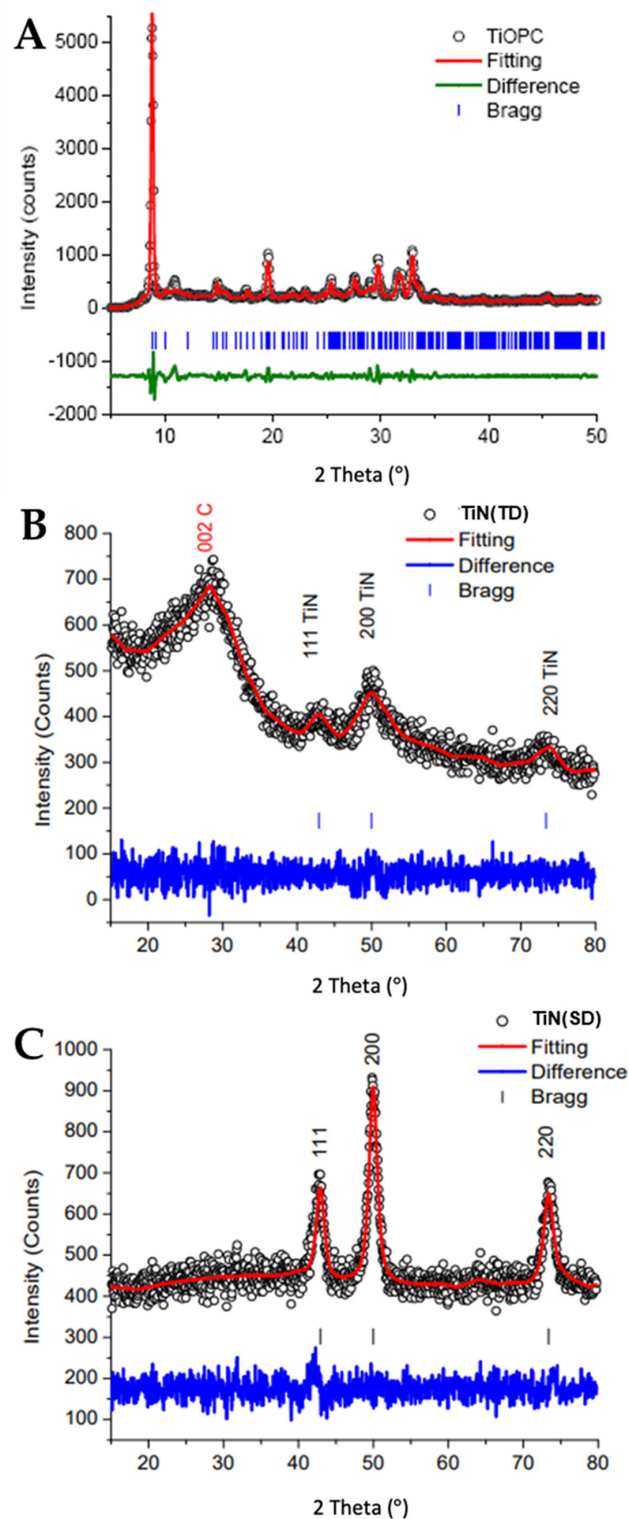


Figure 4. XRD patterns for (A) TiOPC, (B) TiN(TD), and (C) TiN(SG).

Table 2. Le Bail fitting results for TiOPC, TiN(SG), and TiN(TD).

Compound	Space Group	a (Å)	b (Å)	c (Å)	α (°)	β (°)	γ (°)	* χ^2	Reference
α - H ₂ PC _{syn}	C ₂ /n	25.755	3.773	23.398	90	93.111	90	2.07	This Work
α -H ₂ PC _{lit}	C ₂ /n	26.121	3.797	23.875	90	94.16	90	** N/A	[32]
TiOPC _{syn}	P-1	12.269	12.598	8.594	95.067	96.127	67.818	3.74	This Work
TiOPC _{lit}	P-1	12.17	12.58	8.64	95	96.3	67.9	N/A	[33]
TiN(TD)	FM3-M	4.24 (0)	4.24 (0)	4.24 (0)	90.0	90.0	90.0	1.05	This Work
TiN(SG)	FM3-M	4.24 (0)	4.24 (0)	4.24 (0)	90.0	90.0	90.0	1.50	This Work
TiN _{lit}	FM3-M	4.244	4.244	4.244	90.0	90.0	90.0	N/A	[34]

Note: * is the Chi squared value which is an indicator of the goodness of fit and ** N/A means Not Applicable.

The results of the TiOPC fitting showed that the crystal was in a P-1 lattice, which was consistent with the space group identified in the literature [32]. It can be seen in Table 2 that the calculated lattice parameters were similar to those reported [33]. The lattice parameters of the TiN(SG) prepared using alkoxide-urea confirmed the formation of TiN. More importantly, the crystal lattice for TiN was determined to be FM3-M, a cubic lattice with $a = b = c = 4.240$ Å and $\chi^2 = 1.50$, in close agreement with literature values [34]. TiN(TD) also showed a cubic lattice FM3-M, with $a = b = c = 4.240$ Å and $\chi^2 = 1.05$, also in excellent agreement with results reported for TiN [34]. TiN(TD) showed the presence of amorphous carbon; the 002 peak for amorphous carbon was observed in the diffraction pattern around $2\theta = 28^\circ$. The XRD results for both TiN(SG) and TiN(TD) showed the presence of the 111, 200, and 220 diffraction planes at 42.920 , 49.978 , and 73.372° in 2θ , respectively. The average grain size, determined using Scherrer's equation and corrected for instrumental line broadening, was 7.97 ± 0.4 nm for TiN(SG) and 4.3 ± 0.9 for TiN(TD). The average grain size of TiN(TD) agreed with the values obtained from the TEM results.

3.5. XPS

Figures 5–7 show high-resolution XPS spectra for TiN(SG), TiOPC, and TiN(TD), respectively. Table 3 shows the composition of the samples as determined from the XPS analysis based on atomic percentages. As can be seen in Table 3, the composition of all samples shows a low percentage of titanium. However, the percentage composition of TiN(TD) is approximately twice that observed in the TiOPC sample, which was expected due to the loss of hydrogen and carbon from the material during the carbonization process. Also, the amount of oxygen present in the sample increased, which is more than likely due to the adsorption of oxygen at the surface of the material. The amount of O₂ present in TiN(SG) was also high, which is likely due to surface adsorption of O₂ by the material.

Table 3. Composition of the synthesized nanomaterials as determined from XPS analysis of the samples.

Sample	%Ti	%N	%C	%O
TiOPC	0.6	11.3	81.7	6.4
TiN(TD)	1.3	5.0	82.5	11.3
TiN(SG)	16.1	12.5	52.2	19.2

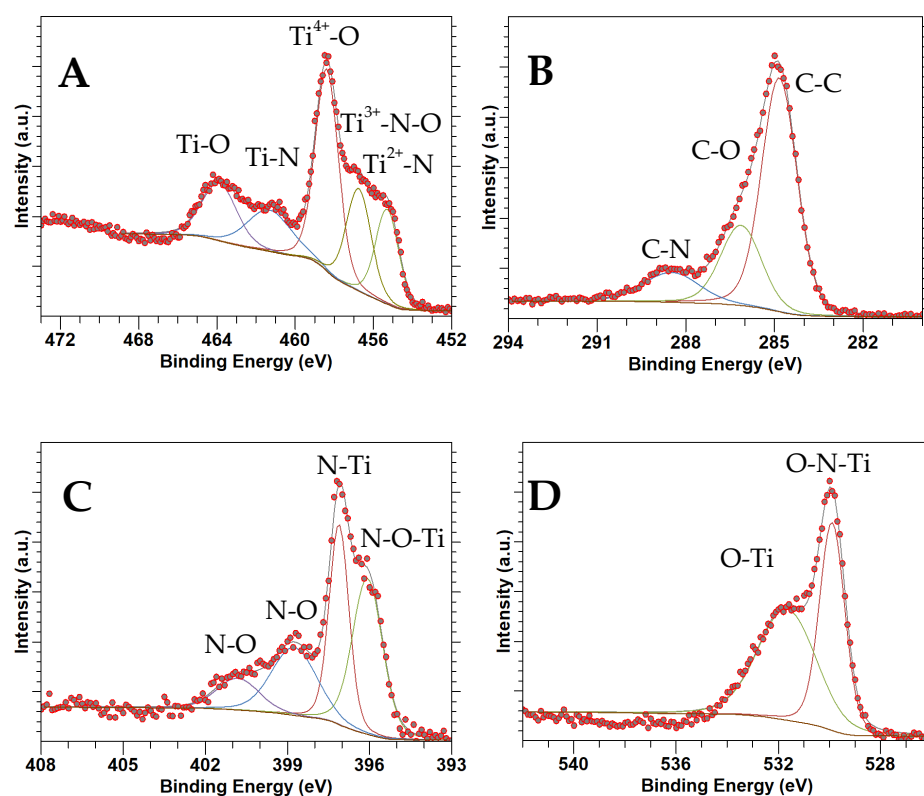


Figure 5. XPS spectra of TiN(SG): (A) Ti 2p, (B) C 1s, (C) N 1s, (D) O 1s.

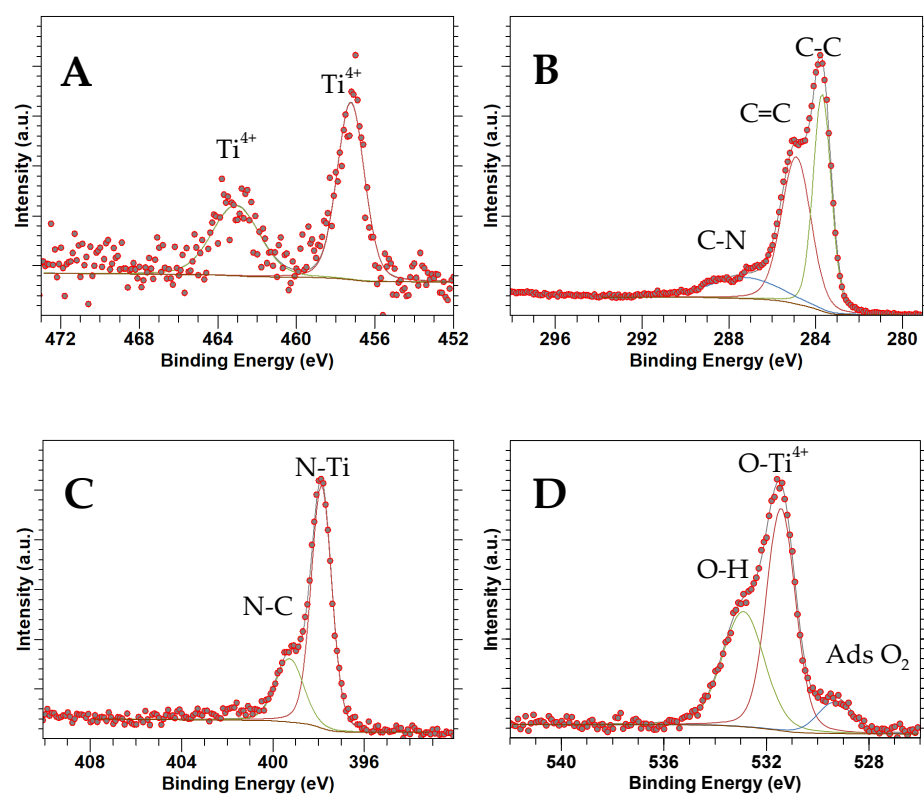


Figure 6. XPS spectra of TiOPC: (A) Ti 2p, (B) C 1s, (C) N 1s, (D) O 1s.

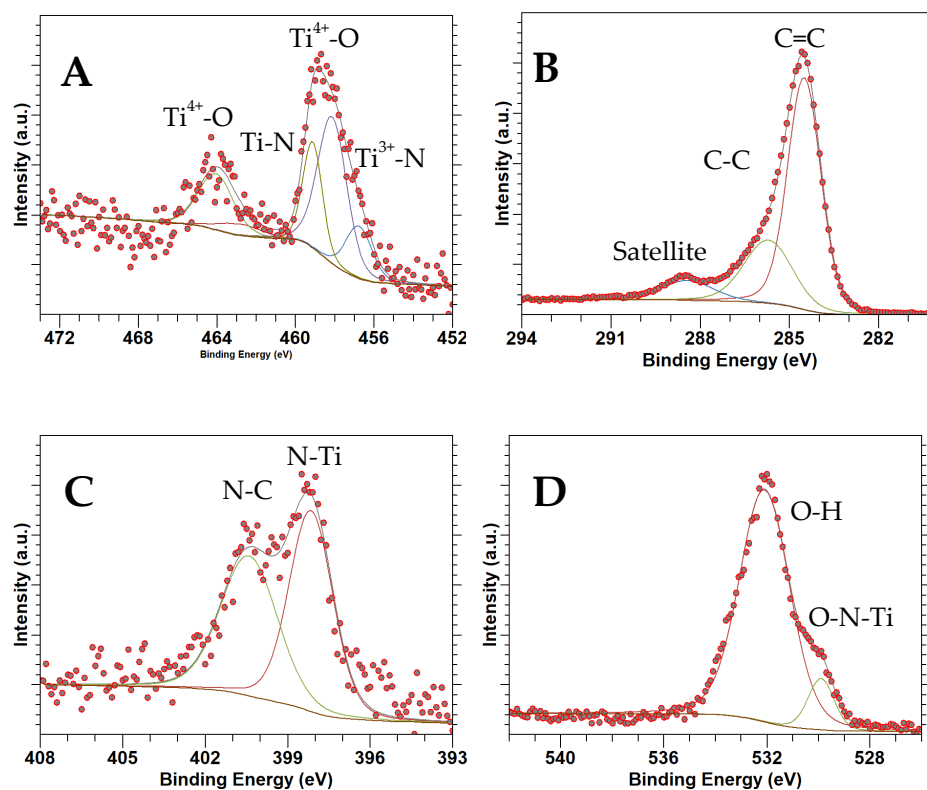


Figure 7. XPS spectra of TiN(TD): (A) Ti 2p, (B) C 1s, (C) N 1s, (D) O 1s.

Figure 5A shows the Ti 2p XPS data for TiN(SG), indicating the existence of Ti $2p_{3/2}$ and Ti $2p_{1/2}$ regions. The Ti $2p_{3/2}$ region was deconvoluted into three components at 455.3, 456.7, and 458.4 eV, corresponding to $Ti^{3+}-N$, $Ti^{3+}-N-O$, and $Ti^{4+}-O$ binding environments, respectively [43–45]. The results indicate that the surface of the TiN has been oxidized. The surface oxidation of TiN(SG) was expected due to the small size of the TiN nanoparticles, determined by XRD to be about 8 nm and calculated based on the average of the peak width of TiN diffraction. Small nanoparticles are typically reactive and undergo surface oxidation readily. However, oxidation was not too extensive, as it was not apparent in the XRD. The Ti $2p_{1/2}$ portion of the spectrum had low intensity and was deconvoluted into two peaks at 461.3 eV and 463.9 eV, corresponding to the Ti-N and Ti-O binding environments, respectively [46]. In addition, the peak representing the Ti-N-O binding environment was not observed. Figure 6A represents the Ti $2p_{3/2}$ and Ti $2p_{1/2}$ XPS of the TiOPC complex. A single peak was identified in the Ti $2p_{3/2}$ region at 457.2 eV, while the Ti $2p_{1/2}$ region exhibited a peak at 463.1 eV. This alignment is consistent with the presence of Ti^{4+} , indicating the presence of TiOPC, as reported in the literature [47,48]. Figure 7A shows the Ti 2p spectrum obtained for the TiN(TD) complex. The Ti $2p_{3/2}$ signal was deconvoluted into three peaks at 456.7, 458.1, and 459.1 eV, identified as the $Ti^{3+}-N$, $Ti^{3+}-N-O$, and $Ti^{4+}-O$ binding environments, respectively [45,49]. The binding energies were shifted slightly due to the particle size of 4.3 nm. The shift in the peak positions to higher energies was observed for nanocrystals due to surface strain and surface defects [50,51]. The Ti $2p_{1/2}$ signal was deconvoluted into two peaks at 462.9 and 464.2, indicating the presence of TiN and TiO, respectively [52].

Figure 5B shows the C 1s XPS spectrum collected from TiN(SG). Only one region was present and deconvoluted into three peaks at 284.8, 286.1, and 288.5 eV, corresponding to C-C, C-O, or C-N, and the C satellite peak, respectively [42]. Figure 6B shows the C 1s spectra for the TiOPC complex. The C 1s spectrum was deconvoluted into four peaks at binding energies of 283.7, 284.9, and 287.4 eV, corresponding to the C-C, C=C, and C-N bonds, respectively [53]. Figure 7B shows the C 1s spectra for TiN(TD). The sample was deconvoluted into three peaks located at binding energies of 284.5, 285.7, and 288.4,

corresponding to C=C, C-C, and a satellite peak, respectively [42,54]. There is no indication of the formation of Ti-C, which would be located at a binding energy of 281.8 eV [55], indicating that the sample is a mixture of TiN and carbon. Neither of the synthesized TiN samples showed the presence of TiC, indicating no TiC formed in the conversion process [56].

Figure 5C shows the N 1s region for TiN(SG). The N 1s spectrum consists of four peaks located at 396.1, 397.1, 398.8, and 400.8, identified as N-O-Ti, N-Ti, N-O, and N-O, respectively [48]. Figure 6C shows the N 1s spectrum for the TiOPC complex, which was deconvoluted into two peaks at 397.9 and 399.3 eV, assigned to the N-Ti and N-C binding environments of phthalocyanine, respectively [57]. Figure 7C shows the N 1s XPS spectrum for TiN(TD). The XPS spectrum of the TiN(TD) sample was deconvoluted into two peaks located at 398.2 eV and 400.5 eV. The two peaks observed in the N1s spectrum corresponded to the N-Ti and N-C binding environments [44,46].

Figure 5D shows the O 1s XPS spectrum for TiN(SG), which was deconvoluted into two individual peaks at 529.9 and 531.7 eV, determined to be the O₂ adsorbed and the O-N-Ti oxygen environments, respectively [46,58]. These results are consistent with the binding environments observed in the Ti 2p for TiN(SG). Figure 6D shows the O 1s XPS spectra for the TiOPC complex, which was deconvoluted into three peaks at 529.3, 531.4, and 532.9 eV, which were determined to be adsorbed oxygen, the oxygen bound to Ti (IV), indicating the formation of titanyl phthalocyanine (TiOPC), and the presence of water/hydroxide in the sample [58,59]. Figure 7D shows the O 1s spectrum of TiN(TD). The O 1s spectrum consisted of two peaks located at 529.9 and 532.2 eV, which were determined to be oxygen adsorbed and O-N-Ti and the presence of hydroxide or water in the sample [45,58]. The results of the XPS fittings are summarized in Table 4.

Table 4. A summary of the XPS fitting results for each of the elements observed in the samples.

Sample	Ti 2p _{3/2}	Energy (eV)	Ti2P _{1/2}	O 1s	Energy (eV)	N1S	Energy (eV)	C 1s	Energy (eV)
TiOPC	Ti ⁴⁺ -N/O	457.2	463.1	O-Ti	529.3	N-Ti	397.9	C-C	283.7
				O-H	531.4	N-C	399.3	C=C	284.9
				O _{2ads}	532.9			C-N	287.4
TiN(TD)	Ti-N	456.7	462.9	O-N-Ti	529.9	N-Ti	398.2	C-C	284.5
	Ti-N-O	458.1		O-H	532.2	N-C	400.5	C-O/C-N	285.7
	Ti-O	459.1	464.2					Satellite	288.4
TiN(SG)	Ti-N	455.5	461.3	O _{2ads}	529.9	N-O-Ti	396.1	C-C	284.8
	Ti-N-O	456.7		O-N-Ti	531.7	N-Ti	397.1	C-O/C-N	286.1
	Ti-O	458.4	469.3			N-O	398.8	Satellite	288.4
						N=O	400.8		

4. Cyclic Voltammetry

Cyclic voltammetry (CV) measurements of the initial three cycles for thermally decomposed H₂PC (H₂PC(TD)) and TiN(TD) are shown in Figure 8. The experimental data were collected over a potential window between 0.05 and 3.0 V (vs. Li⁺/Li) at a scan rate of 0.2 mVs⁻¹. Figure 9A shows a difference between the first and second cycles due to the formation of the solid electrolyte interface (SEI) layer at the first cathodic scan (lithiation). The second and subsequent cycles overlap, indicating good reversibility and high coulombic efficiency. The anodic peaks observed at 2.5 V correspond to the pyrolysis of the polyacrylonitrile binder during the heat treatment of the slurry [60]. The thermal decomposition of H₂PC and thermal treatment performed on its slurry resulted in the formation of a carbon electrode. The peak around 0.5 V observed on the first cathodic scan indicates the formation of the SEI layer, while the anodic peaks around 1 V indicate the intercalation between Li⁺ and carbon.

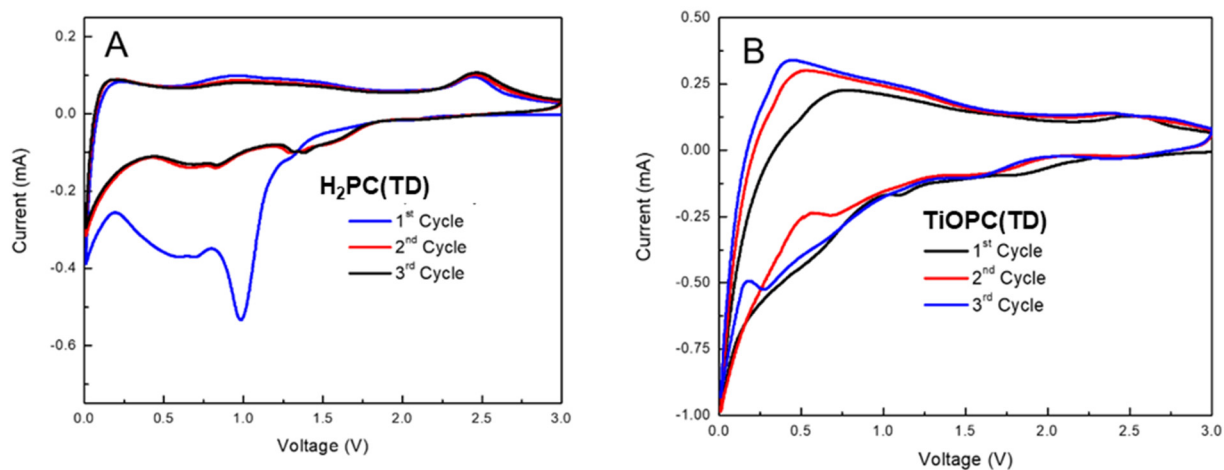


Figure 8. Cyclic voltammetry curves of (A) H₂PC(TD) and (B) TiN(TD) electrode materials.

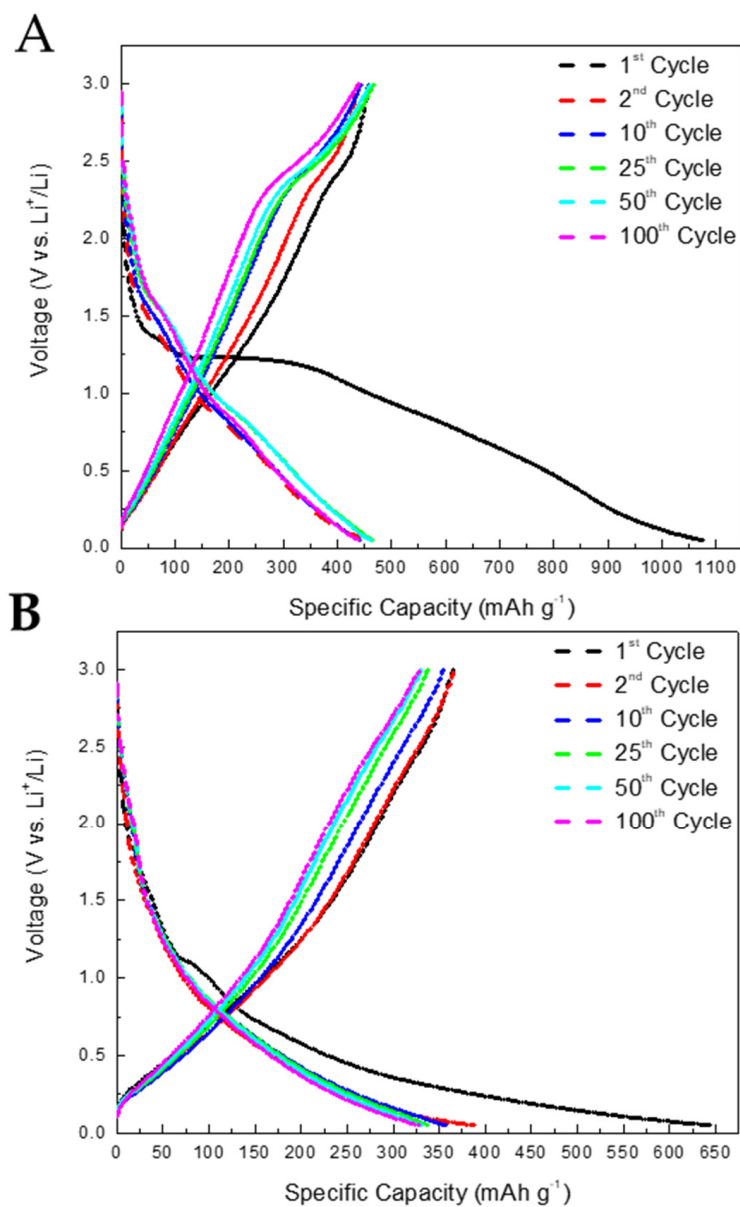


Figure 9. (A) Charge/discharge curves at a current density of 100 mA g⁻¹ H₂PC(TD). (B) Charge/discharge curves of TiN(TD) anode at a current density of 100 mA g⁻¹.

TiN(TD), depicted in Figure 8B, exhibits a difference between the first and second cycles, which is also attributed to the SEI formation. The small cathodic peak around 0.6 V is indicative of the SEI layer formation at the first discharge process. Multiple cathodic peaks were observed in the first discharge process (lithiation), indicating a complex reaction between TiN and Li. It is also worthwhile to mention that the electrode contained a substantial amount of carbon because of the synthesis method and thermal treatment process performed on the starting materials (slurry), which may result in a complicated CV profile. The cathodic and anodic peaks around 0.5 V are assigned to the lithiation and delithiation of the carbon phase in the electrode, respectively [61].

Figure 9A,B shows the galvanostatic charge/discharge curves of H₂PC(TD) and TiN(TD) anodes after 100 cycles at a current density of 100 mA g⁻¹ within a voltage window of 0.1–3 V. Both anodes show high irreversible capacities at the first discharge (Li-insertion) cycle. The irreversible capacity may be caused by the reductive decomposition of electrolyte solution and the subsequent formation of the SEI layer at the anode surface. However, the TiN(TD) anode showed a lower irreversible capacity at the first charge cycle (44% loss in capacity) than that observed for the H₂PC(TD) anode (58% loss). The capacity retention after the second cycle for both electrodes was good (almost 100%), resulting in a high coulombic efficiency of nearly 100%, indicating the formation of a stable interface (SEI layer) during subsequent charge-discharge cycles.

Figure 10 shows the cycle performance and coulombic efficiency of H₂PC(TD) and TiN(TD) electrodes after 100 cycles at 100 mA g⁻¹. The H₂PC(TD) anode exhibited a stable charge capacity, which is consistent with the observation that the H₂PC(TD) anode exhibits a higher theoretical capacity than TiN(TD). After the fifth cycle, the capacity of the H₂PC(TD) anode started to increase, and after 30 cycles, the capacity was decreased to 420 mA h g⁻¹ and remained stable up to 100 cycles. On the other hand, the charge capacity of the TiN(TD) electrode decreased after a few cycles and then remained constant at 350 mA h g⁻¹ after 100 cycles, indicating good electrochemical stability. The TiN(TD) anode exhibits higher initial coulombic efficiency (56.1%) and better capacity retention (98.3% of the second cycle) than the H₂PC(TD) anode. The improvement of TiN(TD) capacity compared to commercial graphite anode or carbon fiber anodes might be due to the synergistic effect of TiN on the electrochemical performance of the carbon matrix anode and might also be due to the good electrical conductivity and high chemical and thermal stability of TiN. However, pure TiN suffers from irreversible oxidation reactions, which lead to poor cyclability [62]. For this reason, the addition of conductive carbon to TiN can prevent the oxidation reaction and improve the cyclability of the TiN anode [62]. In fact, there is a contribution from TiN and carbon to the capacity observed for the TiN(TD) anode. Previous experiments performed on carbon-fiber anodes under the same conditions (current density of 100 mA h g⁻¹) have shown the capacity of the carbon-fiber anode was approximately 200 mA h g⁻¹ after 100 cycles, which is lower than those observed in the present work [63–65]. TiN has been used as a coating material for high-capacity anodes in LIBs such as Si and SnO₂ [66,67]. The TiN/Si and TiN/SnO₂ composite anodes exhibited good electrochemical performance compared to the Si and SnO₂ anodes. This was in part due to the good electrical conductivity and chemical and thermal stability of TiN [66,67].

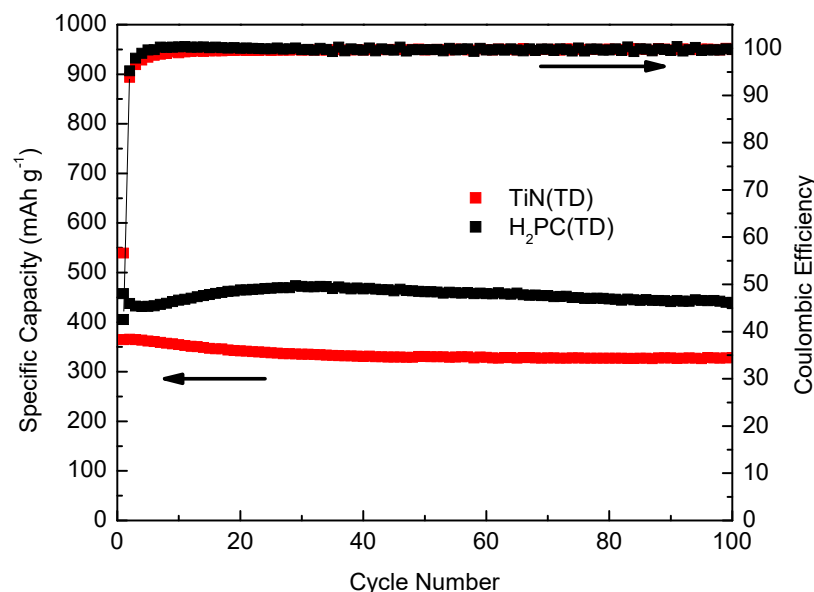


Figure 10. Electrochemical performance and coulombic efficiency of thermally carbonized metal-free phthalocyanine and titanium phthalocyanine electrode materials.

5. Conclusions

The thermal decomposition of TiOPC turned out to be a facile, rapid, and effective process for preparing anode materials for LIBs, offering the advantages of using precursors fabricated by well-known compounds with a long shelf life and good chemical stability. In addition, the material showed the presence of small TiN nanoparticles approximately 3–4 nm in size attached to the carbon matrix. The nanoparticles were present in clusters of small spherical particles observed throughout the material. The composition of the nanoparticles was confirmed by XPS and XRD, which showed the presence of TiN and no evidence of the synthesis of TiC (as a by-product). The electrochemical performance showed both the carbon synthesized from the H₂PC and the TiN(TD) materials had high cycle stability and excellent electrochemical performance with a stable capacity over 100 cycles at 100 mA g⁻¹. The potential exists for a carbon-stabilized TiN material to be easily synthesized for LIB anode applications.

Author Contributions: Conceptualization, H.M.M., M.A. and J.G.P.; Methodology, H.M.M., M.A. and J.G.P.; Formal Analysis, H.M.M., M.A., E.M.F., D.A.S., H.V., V.P.-G., M.O. and J.G.P.; Investigation, H.M.M., D.A.S., E.M.F., M.O. and V.P.-G.; Resources, H.M.M., M.A., T.P.L. and J.G.P.; Data Curation, M.A. and J.G.P.; Writing—Original Draft Preparation, H.M.M.; Writing—Review & Editing, H.M.M., H.V., V.P.-G., M.O., T.P.L., M.A. and J.G.P.; Visualization, H.M.M.; Supervision, M.A. and J.G.P.; Project Administration, J.G.P.; Funding Acquisition, T.P.L., M.A., H.M.M. and J.G.P. All authors have read and agreed to the published version of the manuscript.

Funding: H.M. Morales and J.G. Parsons acknowledge and are grateful for the support provided by the UTRGV Chemistry Departmental Welch Foundation Grant (Grant No. BX-0048), and M. Alcoutlabi acknowledges funding from NSF PREM (DMR-2122178), Partnership for Fostering Innovation by Bridging Excellence in Research and Student Success. Part of this work was carried out in the College of Science and Engineering Characterization Facility, University of Minnesota, which has received capital equipment funding from the NSF through the UMN MRSEC program under Award Number DMR-2011401.

Data Availability Statement: All the relevant data that support the findings of this study are available from the corresponding authors on reasonable request.

Conflicts of Interest: The authors declare no conflict of interest.

References

1. Togonon, J.J.; Chiang, P.-C.; Lin, H.-J.; Tsai, W.-C.; Yen, H.-J. Pure carbon-based electrodes for metal-ion batteries. *Carbon Trends* **2021**, *3*, 100035. [[CrossRef](#)]
2. Yao, F.; Pham, D.T.; Lee, Y.H. Carbon-Based Materials for Lithium-Ion Batteries, Electrochemical Capacitors, and Their Hybrid Devices. *ChemSusChem* **2015**, *8*, 2284–2311. [[CrossRef](#)] [[PubMed](#)]
3. Yue, Y.; Han, P.; Dong, S.; Zhang, K.; Zhang, C.; Shang, C.; Cui, G. Nanostructured transition metal nitride composites as energy storage material. *Chin. Sci. Bull.* **2012**, *57*, 4111–4118. [[CrossRef](#)]
4. Wang, P.; Zhao, B.; Bai, J.; Tong, P.; Zhu, X.; Sun, Y. Transition Metal Nitrides in Lithium- and Sodium-Ion Batteries: Recent Progress and Perspectives. *Adv. Mater. Interfaces* **2022**, *9*, 2200606. [[CrossRef](#)]
5. Wang, L.; Zheng, H.; Jin, X.; Yuan, Y. Fe₃O₄ Hollow Nanospheres Grown In Situ in Three-Dimensional Honeycomb Macroporous Carbon Boost Long-Life and High-Rate Lithium Ion Storage. *J. Electron. Mater.* **2023**, *52*, 10–22. [[CrossRef](#)]
6. Zhang, H.; Zhao, H.; Khan, M.A.; Zou, W.; Xu, J.; Zhang, L.; Zhang, J. Recent progress in advanced electrode materials, separators and electrolytes for lithium batteries. *J. Mater. Chem. A* **2018**, *6*, 20564–20620. [[CrossRef](#)]
7. Zubi, G.; Dufo-López, R.; Carvalho, M.; Pasaoglu, G. The lithium-ion battery: State of the art and future perspectives. *Renew. Sustain. Energy Rev.* **2018**, *89*, 292–308. [[CrossRef](#)]
8. Li, J.A.; Fleetwood, J.; Hawley, W.B.; Kays, W. From Materials to Cell: State-of-the-Art and Prospective Technologies for Lithium-Ion Battery Electrode Processing. *Chem. Rev.* **2022**, *122*, 903–956. [[CrossRef](#)]
9. Nandi, D.K.; Sen, U.K.; Choudhury, D.; Mitra, S.; Sarkar, S. Atomic Layer Deposited Molybdenum Nitride Thin Film: A Promising Anode Material for Li Ion Batteries. *ACS Appl. Mater. Interfaces* **2014**, *6*, 6606–6615. [[CrossRef](#)] [[PubMed](#)]
10. Gillot, F.; Oró-Solé, J.; Palacín, M.R. Nickel nitride as negative electrode material for lithium ion batteries. *J. Mater. Chem.* **2011**, *21*, 9997–10002. [[CrossRef](#)]
11. Tang, D.; Yi, R.; Gordin, M.L.; Melnyk, M.; Dai, F.; Chen, S.; Song, J.; Wang, D. Titanium nitride coating to enhance the performance of silicon nanoparticles as a lithium-ion battery anode. *J. Mater. Chem.* **2014**, *2*, 10375–10378. [[CrossRef](#)]
12. Balogun, M.-S.; Li, C.; Zeng, Y.; Yu, M.; Wu, Q.; Wu, M.; Lu, X.; Tong, Y. Titanium dioxide@titanium nitride nanowires on carbon cloth with remarkable rate capability for flexible lithium-ion batteries. *J. Power Sources* **2014**, *272*, 946–953. [[CrossRef](#)]
13. Zheng, H.; Fang, S.; Tong, Z.; Pang, G.; Shen, L.; Li, H.; Yang, L.; Zhang, X. Stabilized titanium nitride nanowire supported silicon core-shell nanorods as high capacity lithium-ion anodes. *J. Mater. Chem. A* **2015**, *3*, 12476–12481. [[CrossRef](#)]
14. Dong, S.; Chen, X.; Gu, L.; Zhou, X.; Xu, H.; Wang, H.; Lui, Z.; Han, P.; Yao, J.; Wang, L.; et al. Facile Preparation of Mesoporous Titanium Nitride Microspheres for Electrochemical Energy Storage. *ACS Appl. Mater. Interfaces* **2011**, *3*, 93–98. [[CrossRef](#)] [[PubMed](#)]
15. Agrafiotis, C.C.; Puszynski, J.A.; Lavacek, V.H. Experimental Study on the Synthesis of Titanium and Tantalum Nitrides in the Self-Propagating Regime. *Combust. Sci. Technol.* **1991**, *76*, 187–218. [[CrossRef](#)]
16. Giordano, C.; Erpen, C.; Yao, W.; Milke, B.; Antonietti, M. Metal Nitride Metal Carbide Nanoparticles by a Soft Urea Pathway. *Chem. Mater.* **2009**, *21*, 5136–5144. [[CrossRef](#)]
17. Combadiere, L.; Machet, J. Reactive magnetron sputtering deposition of TiN films. II. Influence of substrate temperature on the mechanical properties of the films. *Surf. Coat. Technol.* **1997**, *88*, 28–37. [[CrossRef](#)]
18. Bhaskar, U.; Bid, S.; Satpati, B.; Pradhan, S. Mechanochemical synthesis of nanocrystalline titanium nitride and its microstructure characterization. *J. Alloys Compd.* **2010**, *493*, 192–196. [[CrossRef](#)]
19. Cai, P.-J.; Li, G.-Z.; Shi, C.; Huo, J.-H.; Liu, L.-H. A Low Temperature Synthetic Route to Nanocrystalline TiN. *S. Afr. J. Chem.* **2011**, *64*, 57–60.
20. White, G.V.; Mackenzie, K.J.; Brown, I.W.; Bowden, M.E.; Johnston, J.H. Carbothermal synthesis of titanium nitride. *J. Mater. Sci.* **1992**, *27*, 4294–4299. [[CrossRef](#)]
21. Grillo, A.; Moura, F.; Solorzano, G.; Brocchi, E.; Mendoza Oliveros, M. Vapour Phase Synthesis and Characterization of TiN Nanoparticles. *Chem. Eng. Trans.* **2017**, *57*, 1399–1404.
22. Kaskel, S.A.; Schlichte, K.; Chaplais, G.; Khanna, M. Synthesis and characterisation of titanium nitride based nanoparticles. *J. Mater. Chem.* **2003**, *13*, 1496–1499. [[CrossRef](#)]
23. Schaaf, P.; Kahle, M.; Carpenne, E. Reactive laser synthesis of carbides and nitrides. *Appl. Surf. Sci.* **2005**, *247*, 607–615. [[CrossRef](#)]
24. Vaidhyanathan, B.; Rao, K.J. Synthesis of Ti, Ga, and V Nitrides: Microwave-Assisted Carbothermal Reduction and Nitridation. *Chem. Mater.* **1997**, *9*, 1196–1200. [[CrossRef](#)]
25. Wade, T.; Ross, C.B.; Crooks, R.M. Electrochemical Synthesis of Ceramic Materials. 5. An Electrochemical Method Suitable for the Preparation of Nine Metal Nitrides. *Chem. Mater.* **1997**, *9*, 248–254. [[CrossRef](#)]
26. Fix, R.; Gordon, R.G.; Hoffman, D.M. Chemical vapor deposition of vanadium, niobium, and tantalum nitride thin films. *Chem. Mater.* **1993**, *5*, 614–619. [[CrossRef](#)]
27. Gajbhiye, N.; Ningthoujam, R. Low temperature synthesis, crystal structure and thermal stability studies of nanocrystalline VN particles. *Mater. Res. Bull.* **2006**, *41*, 1612–1621. [[CrossRef](#)]
28. Gomathi, A.; Rao, C. Nanostructures of the binary nitrides, BN, TiN, and NbN, prepared by the urea-route. *Mater. Res. Bull.* **2006**, *41*, 941–947. [[CrossRef](#)]

29. Morlanés, N.; Almaksoud, W.; Rai, R.K.; Ould-Chikh, S.; Ali, M.M.; Vidjayacoumar, B.; Al-Sabban, B.E.; Albahily, K.; Basset, J.-M. Development of catalysts for ammonia synthesis based on metal phthalocyanine materials. *Catal. Sci. Technol.* **2020**, *10*, 844–852. [CrossRef]
30. Sanchez-Sanchez, A.; Izquierdo, M.T.; Mathieu, S.; Ghanbaja, J.; Celzard, A.; Fierro, V. Structure and electrochemical properties of carbon nanostructures derived from nickel(II) and iron(II) phthalocyanines. *J. Adv. Res.* **2020**, *22*, 85–97. [CrossRef]
31. Goedken, V.L.; Dessy, G.; Ercolani, C.; Fares, V. Synthesis, reactivity, and X-ray crystal structure of dichloro(phthalocyaninato)titanium(IV). *Inorg. Chem.* **1985**, *24*, 991–995. [CrossRef]
32. Li, X.; Feng, Y.; Li, C.; Han, H.; Hu, X.; Ma, Y.; Yang, Y. One-step preparation of metal-free phthalocyanine with controllable crystal form. *Green Process. Synth.* **2021**, *10*, 95–100. [CrossRef]
33. Hiller, W.; Strähle, J.; Kobel, W.; Hanack, M. Polymorphie, Leitfähigkeit und Kristallstrukturen von Oxo-phthalocyaninato-titan(IV). *Z. Kristallogr. Cryst. Mater.* **1982**, *159*, 173–184. [CrossRef]
34. Brager, A. An X-ray examination of titanium nitride. *Acta Physicochim.* **1939**, *9*, 617–632.
35. Rodríguez-Carvajal, J. Recent advances in magnetic structure determination by neutron powder diffraction. *Physica B* **1993**, *192*, 55–69. [CrossRef]
36. Fairley, N.; Fernandez, V.; Richard-Plouet, M.; Guillot-Duendon, C.; Walton, J.; Smith, E.; Flahaut, D.; Greiner, M.; Biesinger, M.; Tougaard, S.; et al. Systematic and collaborative approach to problem solving using X-ray photoelectron spectroscopy. *Appl. Surf. Sci. Adv.* **2021**, *5*, 100112. [CrossRef]
37. Harbeck, S.; Mack, H. Experimental and Theoretical Investigations on the IR and Raman Spectra for CuPc and TiOPc; Universität Tübingen. 2013, pp. 1–19. Available online: <http://hdl.handle.net/10900/49961> (accessed on 17 January 2024).
38. Seoudi, R.; El-Bahy, G.; El Sayed, Z. FTIR, TGA and DC electrical conductivity studies of phthalocyanine and its complexes. *J. Mol. Struct.* **2005**, *753*, 119–126. [CrossRef]
39. Ahmad, A.; Collins, R.A. FTIR characterization of triclinic lead phthalocyanine. *J. Phys. D* **1991**, *24*, 1894. [CrossRef]
40. Fernandez, L.; Thussing, S.; Mänz, A.; Sundermeyer, J.; Witte, G.; Jakob, P. The discrete nature of inhomogeneity: The initial stages and local configurations of TiOPc during bilayer growth on Ag(111). *Phys. Chem. Chem. Phys.* **2017**, *19*, 2495–2502. [CrossRef]
41. Denekamp, I.M.; Veenstra, F.L.; Jungbacker, P.; Rothenberg, G. A simple synthesis of symmetric phthalocyanines and their respective perfluoro and transition-metal complexes. *Appl. Organomet. Chem.* **2019**, *33*, 4872. [CrossRef]
42. Neamtu, M.A.; Nadejde, C.; Brinza, L.; Dragos, O.; Gherghel, D.; Paul, A. Iron phthalocyanine-sensitized magnetic catalysts for BPA photodegradation. *Sci. Rep.* **2020**, *10*, 5376. [CrossRef]
43. Cheng, H.; Garcia-Araez, N.; Hector, A.L.; Soulé, S. Synthesis of Hard Carbon-TiN/TiC Composites by Reacting Cellulose with TiCl₄ Followed by Carbothermal Nitridation/Reduction. *Inorg. Chem.* **2019**, *58*, 5776–5786. [CrossRef]
44. Jaeger, D.; Patscheider, J. A complete and self-consistent evaluation of XPS spectra of TiN. *J. Electron. Spectrosc. Relat. Phenom.* **2012**, *185*, 523–534. [CrossRef]
45. Shen, H.; Wang, L. Corrosion resistance and electrical conductivity of plasma nitrided titanium. *Int. J. Hydrogen Energy* **2021**, *46*, 11084–11091. [CrossRef]
46. Mucha, N.R.; Som, J.; Shaji, S.; Fialkova, S.; Apte, P.R.; Balasubramanian, B.; Shield, J.E.; Anderson, M.; Kumar, D. Electrical and optical properties of titanium oxynitride thin films. *J. Mater. Sci.* **2020**, *55*, 5123–5134. [CrossRef]
47. Shi, P.; Song, Y.; Tang, J.; Nie, Z.; Chang, J.; Chen, Q.; He, Y.; Guo, T.; Zhang, J.; Wang, H. Ultra-narrow bandwidth red-emission carbon quantum dots and their bio-imaging. *Physica E* **2022**, *142*, 115197. [CrossRef]
48. Scrocco, M.; Paoletti, A.M.; Ercolani, C. Electron Energy Level Transitions in Bis(phthalocyaninato)titanium(IV) Examined by UV–Visible, Near-IR, EELS, and XPS Spectra. *Inorg. Chem.* **1996**, *35*, 4479–4788. [CrossRef]
49. Chan, M.H.; Lu, F.-H. X-ray photoelectron spectroscopy analyses of titanium oxynitride films prepared by magnetron sputtering using air/Ar mixtures. *Thin Solid Films* **2009**, *517*, 5006–5009. [CrossRef]
50. Huizinga, T.; van 't Blik, H.F.J.; Vis, J.C.; Prins, R. XPS investigations of Pt and Rh supported on γ -Al₂O₃ and TiO₂. *Surf. Sci.* **1983**, *135*, 580–596. [CrossRef]
51. Anatoly, I.; Wainstein, D.L.; Rashkovskiy, A.Y.; Oshero, A.; Golan, Y. Size shift of XPS lines observed from PbS nanocrystals. *Surf. Interface Anal.* **2010**, *42*, 850–854.
52. Beaudette, C.A.; Tu, Q.; Ali Eslamisaray, M.; Kortshagen, U.R. Plasma-Synthesized Nitrogen-Doped Titanium Dioxide Nanoparticles with Tunable Visible Light Absorption and Photocatalytic Activity. *ASME Open J. Eng.* **2022**, *1*, 2770–3495. [CrossRef]
53. Farahmand, S.; Ghiaci, M.; Asghari, S. Oxo-vanadium (IV) phthalocyanine implanted onto the modified SBA-15 as a catalyst for direct hydroxylation of benzene to phenol in acetonitrile-water medium: A kinetic study. *Chem. Eng. Sci.* **2021**, *232*, 116331. [CrossRef]
54. Filik, J.; May, P.W.; Pearce, S.R.; Wild, R.K.; Hallam, K.R. XPS and laser Raman analysis of hydrogenated amorphous carbon films. *Diam. Relat. Mater.* **2003**, *12*, 974–978. [CrossRef]
55. Girolami, G.S.; Jensen, J.A.; Pollina, D.M.; Allocca, C.M.; Kaloyeros, A.E.; Williams, W.S. Organometallic route to the chemical vapor deposition of titanium carbide films at exceptionally low temperatures. *J. Am. Chem. Soc.* **1987**, *109*, 1579–1580. [CrossRef]
56. Lewin, E.; Persson, P.; Lattemann, M.; Stüber, M.; Gorgoi, M.; Sandell, A.; Ziebert, C.; Schafers, F.; Braun, W.; Hailbritter, J.; et al. On the origin of a third spectral component of C1s XPS-spectra for nc-TiC/a-C nanocomposite thin films. *Surf. Coat. Technol.* **2008**, *202*, 3563–3570. [CrossRef]

57. Shubina, T.E.; Marbach, H.; Flechtner, K.; Kretschmann, A.; Jux, N.; Buchner, F.; Steinruck, H.-P.; Clark, T.; Gottfried, J.M. Principle and Mechanism of Direct Porphyrin Metalation: Joint Experimental and Theoretical Investigation. *J. Am. Chem. Soc.* **2007**, *129*, 9476–9483. [[CrossRef](#)] [[PubMed](#)]
58. Jones, T.E.; Rocha, T.C.R.; Knop-Gericke, A.; Stampfl, C.; Schlogl, R.; Piccinin, S. Thermodynamic and spectroscopic properties of oxygen atmosphere. *Phys. Chem. Chem. Phys.* **2015**, *17*, 9288. [[CrossRef](#)]
59. Ageeva, T.A.; Golubev, D.V.; Gorshkova, A.S.; Ionov, A.M.; Kopylova, E.V.; Koifman, O.I.; Mozhchil, R.N.; Rozhkova, E.P.; Rumyantseva, V.D.; Sigov, A.S.; et al. XPS and IR Spectroscopic Studies of Titanyl and Vanadyl Complexes. *Macroheterocycles* **2019**, *12*, 148–153. [[CrossRef](#)]
60. Zhang, C.; Yang, F.; Zhang, D.; Xue, C.; Zou, Y.; Li, C.; Chen, B.; Wang, Q. A binder-free Si-based anode for Li-ion batteries. *RSC Adv.* **2015**, *5*, 15940–15943. [[CrossRef](#)]
61. Balogun, M.-S.; Qiu, W.; Wang, W.; Fang, P.; Lu, X.; Tong, Y. Recent advances in metal nitrides as high-performance electrode materials for energy storage devices. *J. Mater. Chem. A* **2015**, *3*, 1364–1387. [[CrossRef](#)]
62. Ji, L.; Meduri, P.; Agubra, V.; Xiao, X.; Alcoutlabi, M. Graphene-Based Nanocomposites for Energy Storage. *Adv. Energy Mater.* **2016**, *6*, 1502159. [[CrossRef](#)]
63. Chavez, R.O.; Lodge, T.P.; Alcoutlabi, M. Recent developments in centrifugally spun composite fibers and their performance as anode materials for lithium-ion and sodium-ion batteries. *Mater. Sci. Eng.* **2021**, *266*, 115024. [[CrossRef](#)]
64. Chavez, R.O.; Lodge, T.P.; Huitron, J.; Chipara, M.; Alcoutlabi, M. Centrifugally spun carbon fibers prepared from aqueous poly(vinylpyrrolidone) solutions as binder-free anodes in lithium-ion batteries. *J. Appl. Polym. Sci.* **2021**, *138*, 50396. [[CrossRef](#)]
65. Agubra, A.; Zuniga, L.; Flores, D.; Campos, H.; Villarreal, J.; Alcoutlabi, M. A comparative study on the performance of binary SnO₂/NiO/C and Sn/C composite nanofibers as alternative anode materials for lithium ion batteries. *Electrochim. Acta* **2017**, *224*, 608–621. [[CrossRef](#)]
66. Kim, I.-S.; Kumta, P.N.; Blomgren, G.E. Si/TiN Nanocomposites Novel Anode Materials for Li-Ion Batteries. *Electrochem. Solid-State Lett.* **2000**, *3*, 493. [[CrossRef](#)]
67. Lui, M.; Li, X.; Ming, H.; Adkins, J.; Zhao, X.; Su, L.; Zhou, Q.; Zheng, J. TiN surface modified SnO₂ as an efficient anode material for lithium ion batteries. *New J. Chem.* **2013**, *37*, 2096–2102.

Disclaimer/Publisher’s Note: The statements, opinions and data contained in all publications are solely those of the individual author(s) and contributor(s) and not of MDPI and/or the editor(s). MDPI and/or the editor(s) disclaim responsibility for any injury to people or property resulting from any ideas, methods, instructions or products referred to in the content.